



Slab-driven flow at the base of the mantle beneath the northeastern Pacific Ocean

Jonathan Wolf*, Maureen D. Long

Department of Earth and Planetary Sciences, Yale University, New Haven, CT, USA



ARTICLE INFO

Article history:

Received 7 February 2022

Received in revised form 22 July 2022

Accepted 27 July 2022

Available online xxxx

Editor: H. Thybo

Keywords:

lowermost mantle

slab-driven flow

seismic anisotropy

shear-wave splitting

computational modeling

northeastern Pacific

ABSTRACT

Flow in the mantle's bottom boundary layer plays an important role in shaping structures and processes in the deep mantle; however, knowledge of lowermost mantle flow patterns remains elusive. In particular, the influence of remnant slabs on lowermost mantle flow is poorly known, although it is likely that slabs play an important role in driving flow and thus in controlling key aspects of lowermost mantle behavior. Measurements of seismic anisotropy can yield relatively direct constraints on slab-induced lowermost mantle flow; however, such observations are challenging to make. We take advantage of the excellent raypath coverage beneath the northeastern Pacific Ocean provided by the USArray deployment in North America to provide detailed sampling of a region that has a long subduction history, with remnant slabs likely impinging on the core-mantle boundary. We present observations of coherent, strong shear wave splitting of SKKS and S_{diff} phases across USArray stations and show through global wavefield modeling that the splitting is due to lowermost mantle anisotropy. A stacking approach enables us to make robust estimates of lowermost mantle splitting parameters, which we model by considering realistic mineral physics scenarios. Under the assumption of simple horizontal shear deformation, our observations are consistent with generally north-south flow directions for either a post-perovskite or a bridgmanite mineralogy; ferropericlasite cannot explain observations. We speculate that this flow is driven by subducting slab remnants impinging on the core-mantle boundary.

© 2022 Elsevier B.V. All rights reserved.

1. Introduction

The mantle beneath the northeastern Pacific Ocean (Fig. 1a,d) has a rich subduction history (e.g., Matthews et al., 2016; Merdith et al., 2021; Suzuki et al., 2021). Remnant slabs that reach the lowermost mantle are visible in tomographic velocity models (e.g., Ritsema et al., 2011; French and Romanowicz, 2014; Durand et al., 2017), due to their thermal contrast with the ambient mantle. Beneath our study region, remnants of the Farallon plate (Lithgow-Bertelloni and Richards, 1998) are likely present. This plate has been nearly completely subducted via the north Pacific subduction zones, whose subduction positions stayed relatively stable during the past 300 million years (e.g., Merdith et al., 2021). Additionally, remnants of the Amusia plate, the Inzanagi plate, and the Moghol-Okhotsk plate (e.g., Merdith et al., 2021) could have plausibly reached the core-mantle boundary (CMB) in this region. While it is challenging to confidently identify the present-day location of individual plate fragments in the lowermost mantle (e.g., van der Hilst et al., 1997; Sigloch et al., 2008), it is likely that the lower-

most mantle structure beneath the northeastern Pacific is dominated by slab remnants impinging on the CMB due to the stability of the circum-Pacific subduction for (at least) the past 300 million years (e.g., Wolf and Evans, 2022).

Measurements of seismic anisotropy (Long, 2009; Long and Becker, 2010) can yield relatively direct constraints on deformation and flow in the mantle. While seismic anisotropy in Earth's crust (e.g., Barruol and Kern, 1996) and the upper mantle (e.g., Chang et al., 2014) are relatively straightforward to constrain, measurements of lowermost mantle anisotropy are more challenging, as they must take into account potential contributions from several anisotropic layers, particularly the upper mantle (Wolf et al., 2022a). There are some indications from several previous studies that the lowermost mantle beneath the eastern Pacific is anisotropic (Long, 2009; Nowacki et al., 2010; Asplet et al., 2020). For example, Asplet et al. (2020) detected SKS-SKKS splitting discrepancies (thought to indicate a contribution from lowermost mantle anisotropy) that they interpreted as an anisotropic region of the D'' layer that extends beneath much of the eastern Pacific Ocean (building on work by Long, 2009). Nowacki et al. (2010) inferred tilted transverse anisotropy in the lowermost mantle anisotropy to the south of our study region, although the S-Sc

* Corresponding author.

E-mail address: jonathan.wolf@yale.edu (J. Wolf).

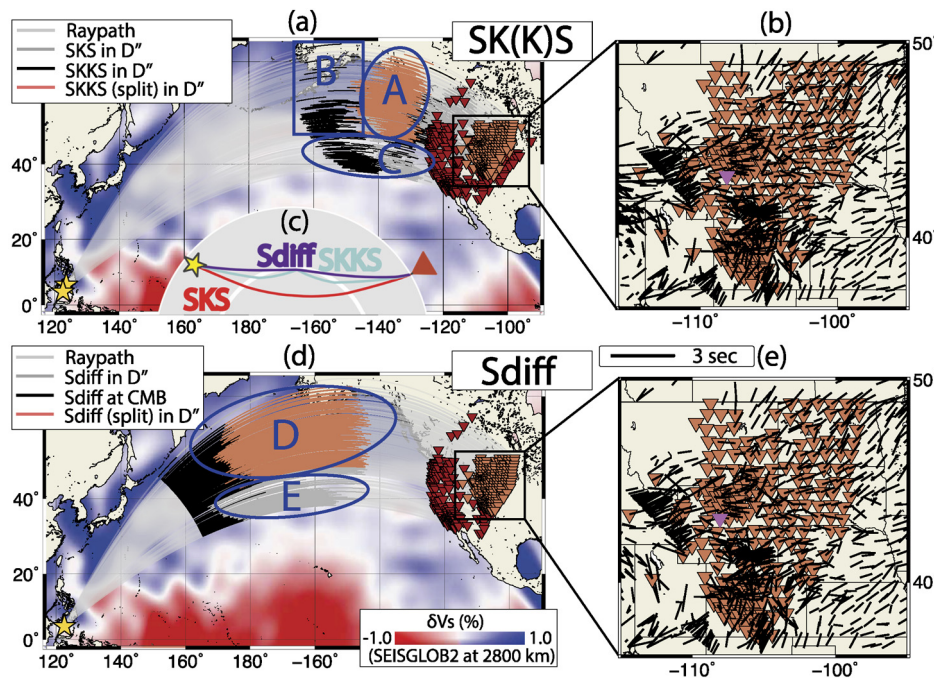


Fig. 1. Raypath and station distribution for SK(K)S phases (a,b) and S_{diff} phases (d,e). Events are represented by yellow stars, stations by dark- and light red triangles. (a) SKS and SKKS raypaths from events 1 and 2. The path length through a 250 km thick D'' is shown in a different color depending on the phase and on whether the phase was split (see legend). Stations are shown in dark red (no splitting observed in record sections shown in S1-S4) or light red (splitting observed). Background colors represent velocity perturbations with respect to PREM (Dziewonski and Anderson, 1981) from SEISGLOB2 (Durand et al., 2017); see color bar at lower right. For better reference in the text, lowermost mantle regions A-C are labeled. (b) Zoomed in map of stations at which splitting due to lowermost mantle anisotropy is observed. The representative station used in the modeling is shown in pink. Black sticks represent upper mantle associated splitting parameters from the IRIS splitting database (Trabant et al., 2012; Liu et al., 2014); the orientation represents the fast polarization direction and the length of the black stick the delay time (legend). (c) Schematic illustration of SK(K)S and S_{diff} raypaths in the Earth. (d) Similar to panel (a) for the S_{diff} phases from event 1. Color of raypath represents path length of S_{diff} along the CMB and through D'' (see legend). Lowermost mantle regions D (splitting observed) and E (no splitting observed) are explained in the text. (e) Similar to panel (b) for those stations that indicate lowermost mantle splitting of S_{diff} . (For interpretation of the colors in the figure(s), the reader is referred to the web version of this article.)

differential splitting technique that they used is based on some restrictive assumptions (Wolf et al., 2022a).

In order to study lowermost mantle anisotropy beneath the northeastern Pacific, we investigate earthquake records with similar raypaths that exhibit particularly clear SKS, SKKS, and S_{diff} arrivals across hundreds of seismic stations in North America. We initially identify a set of seven earthquakes with a source depth >500 km and magnitude $M_w > 6.0$ that occurred below the Celebes Sea in 2009 and 2010 (Supplementary Table S1), when many of the USArray Transportable Array (TA) stations were deployed at epicentral distances between 101° and 120° . We focus on the two highest-quality events from this group, which exhibit high signal-to-noise ratios across a large number of stations (Fig. 1); waveforms from other earthquakes are generally consistent with these two high-quality events, but with substantially higher noise levels. Each of these chosen events is suitable to analyze splitting of SKS and SKKS phases (Fig. 1a), while the initial source polarization is favorable for the analysis of S_{diff} splitting for just one of the events (see Section 3.2). We refer to the earthquake for which S_{diff} could be analyzed as ‘event 1’ (2009-10-07 21:41:14) and the other earthquake as ‘event 2’ (2010-07-24 05:35:01).

We investigate both SKS-SKKS differential splitting and S_{diff} splitting in the waveforms. Large differences in SKS and SKKS splitting for the same event-station pairs are typically inferred to reflect a contribution from D'' anisotropy to the splitting of one or both phases (Long, 2009; Asplet et al., 2020), because the raypaths of these two phases are similar in the upper mantle and diverge substantially in the lowermost mantle (Fig. 1c). The measurement of S_{diff} splitting due to D'' anisotropy is more complicated; while S_{diff} phases are usually mainly SH polarized, it cannot necessarily be assumed that all energy on the radial component of the

seismogram is due to seismic anisotropy (Komatitsch et al., 2010; Borgeaud et al., 2016), and substantial precautions must be taken in order to correctly identify the effect of splitting in S_{diff} waveforms.

2. Methods

2.1. Stacking approach and splitting measurements

Before visual inspection of waveforms, we bandpass filter our data, retaining periods between 8 and 25 s. Then, we conduct a quality check for SK(K)S and S_{diff} to sort out obviously flawed or particularly noisy data (making up less than 30% of our data set). Subsequently, we visualize our data in record sections (e.g., Fig. 2) to detect either a) significantly different transverse energy for SKS compared to SKKS phases, or b) radial energy arriving for S_{diff} that cannot be explained by the initial source polarization. After identifying data with a signature of shear wave splitting due to D'' anisotropy (discussed further in Section 2.1), we linearly stack the aligned data for each phase and event of interest (e.g., Fig. 3) and measure shear wave splitting parameters ϕ' (fast polarization of the wave, measured as an angle from the backazimuthal direction), δt (time lag between the fast and the slow waves) and the splitting intensity (SI ; a measure of the transverse component amplitude, quantifies the degree to which the wave is split; Chevrot, 2000). We obtain these measurements from the stacked data using a modified version of the SplitRacer (Reiss and Rumpker, 2017; Reiss et al., 2019) software (e.g., Fig. 4), using the transverse energy minimization technique (Silver and Chan, 1991) to measure fast direction and delay time, while incorporating a corrected uncertainty estimation (Walsh et al., 2013). SplitRacer includes an automatic

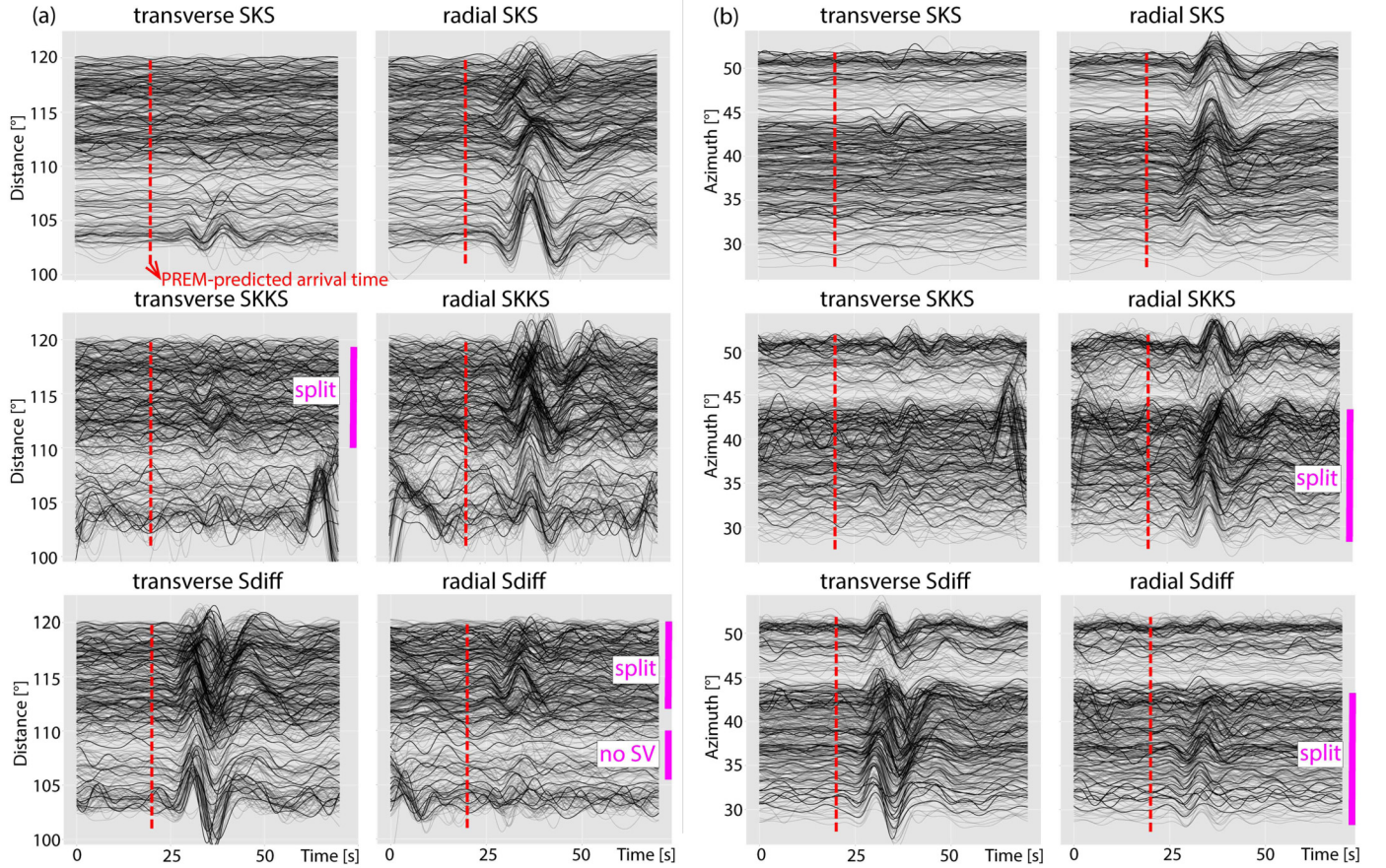


Fig. 2. Waveforms for event 1 (2009-10-07) as a function of distance and azimuth. (a) Record sections of arrivals for SKS (top row), SKKS (middle row) and S_{diff} (bottom row) phases. **Only** every 10th trace is plotted without transparency to better visualize the individual waveforms. Phase arrival times predicted by PREM (Dziewonski and Anderson, 1981) are indicated red dashed lines. The SKKS phases show coherent transverse energy in the distance range between 110° and 119° (pink bar), while the SKS phases do not. The diffracted S waves (bottom row) do not show transverse energy between 107° and 110° distance (pink bar), but do show clear transverse energy for distances larger than 112° (pink bar). (b) Similar representation of waveforms as in panel (a) but as a function of azimuth. For azimuths $<43^\circ$ SKKS is apparently more strongly split than SKS (pink bar). For S_{diff} , clear radial energy is discernible for these azimuths too, while radial energy is less pronounced for larger azimuths.

multi-window calculation of the splitting parameters to avoid bias from manual picking of the measurement window.

2.2. Global wavefield simulations

Our full-waveform simulations using AxiSEM3D (Leng et al., 2016, 2019) are performed using isotropic PREM (Dziewonski and Anderson, 1981) as background model. The general approach to model setup and parameterization is similar to our approach in previous work (Wolf et al., 2022a, 2022b). The lowermost few hundred kilometers of the model are replaced in many of our models by a layer of anisotropy, described by aligned post-perovskite (Ppv)bridgmanite (Br) or ferropericlaite (Fp). Source depths and moment tensors for the events are those reported by the USGS earthquake database. Seismograms are calculated down to periods of 6 s, while paying attention to selecting an appropriately high Fourier expansion order (Leng et al., 2016, 2019; see also Wolf et al., 2022b). Synthetic seismograms are then stacked and evaluated using identical processes as with real data.

For some of our simulations we include anisotropy in both the lowermost mantle and the upper mantle, using the US32 model for azimuthal anisotropy (Zhu et al., 2020). To implement this model into our AxiSEM3D input, we need to produce a full elastic tensor C_{ijkl} based on the parameters used by Zhu et al. (2020) in their model parameterization. In order to create a complete elastic tensor from an azimuthal anisotropy model that does

not fully describe all independent elastic tensor components, we must make some assumptions. We take the following steps: 1) We create a vertical transversely isotropic (VTI) elastic tensor using MSAT (Walker and Wookey, 2012). To do this, we use the shear wave velocity from US32 (Zhu et al., 2020), P-wave velocity from STW105 (Kustowski et al., 2008), $\xi = \frac{V_{SH}^2}{V_{SV}^2}$ from US22 (Zhu et al., 2017), and assume the anisotropic parameters $\eta = \phi = 1$ (implying $V_{PSH} = V_{PSV}$; Panning and Romanowicz, 2006). 2) We mix the elastic tensor obtained in the first step with its isotropic equivalent (calculated using MSAT) to match the anisotropic strength provided by US32 (for each point in the model). 3) We rotate the elastic tensor to have horizontal axis of symmetry (that is, HTI) and 4) rotate the elastic tensor to match its fast direction with that predicted by US32 (for each point in the model). This process yields a full elastic tensor that has the same anisotropy strength and fast axis orientations as the US32 model. We have experimented with changing some of the assumptions made in this process (e.g., assuming the same ξ everywhere in the model space or setting ϕ to other values, thus introducing P-wave anisotropy) to investigate their effects. We found that the details of the assumptions made virtually no difference to the predicted splitting, as expected, because SK(K)S-splitting mainly depends on anisotropic strength and fast S-wave polarization direction (which by design matches US32 in our model).

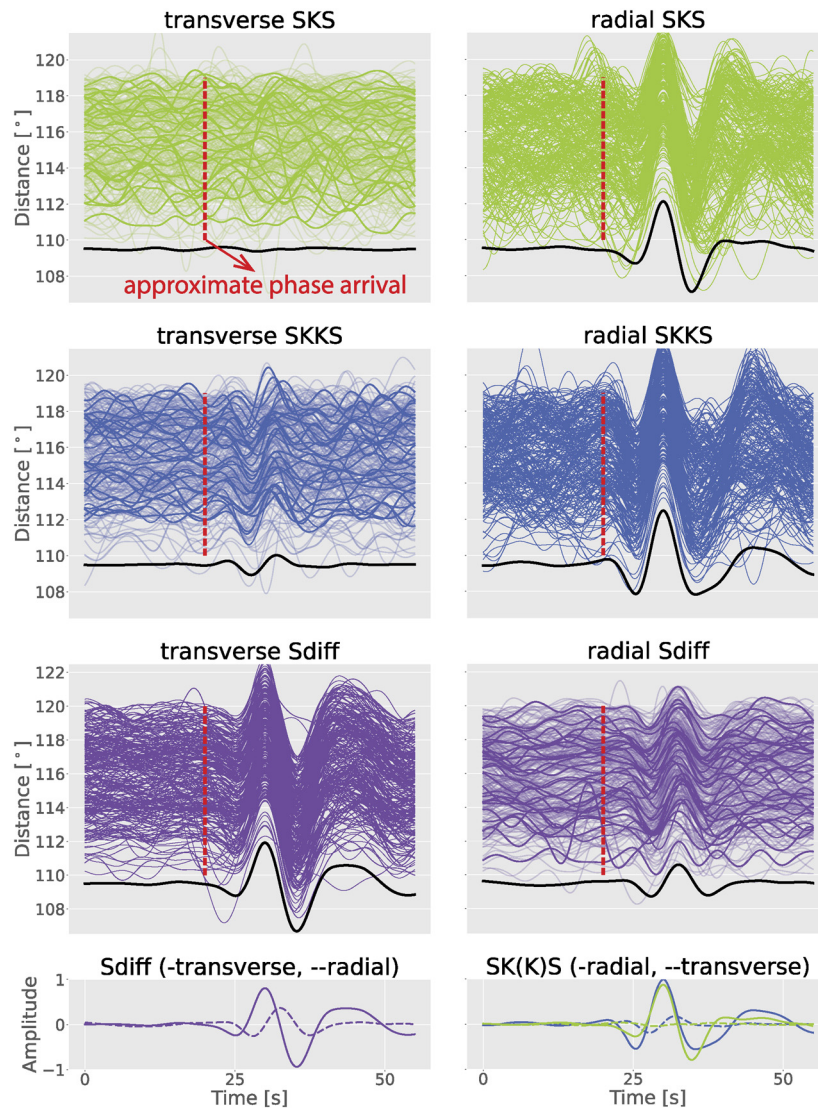


Fig. 3. Transverse and radial component waveforms for SKS (first row), SKKS (second row) and S_{diff} (third row) phases for event 1, aligned and normalized with respect to the maximum radial SK(K)S and maximum transverse S_{diff} amplitudes. For the “split” components (transverse SK(K)S and radial S_{diff}), only every 10th trace is plotted without transparency to better visualize the individual waveforms. Red dashed lines represent the approximate phase arrival times. Stacked traces are plotted in black color on the corresponding panel and again presented in the bottom row (left: S_{diff} ; right: SK(K)S). In contrast to SKKS and S_{diff} , the SKS phases show no signs of coherent splitting – almost no energy arrives on the stacked SKS transverse.

3. Results

In contrast to most D'' anisotropy studies (e.g., Wookey et al., 2005a; Nowacki et al., 2010; Wolf et al., 2019; Asplet et al., 2020), we do not focus on shear wave splitting in single seismograms; rather, we look for evidence of coherent D'' -associated splitting across the hundreds of TA stations by analyzing all the data together (after quality checks; see Section 2.1). We construct record sections, both as a function of distance and azimuth (Fig. 2 and Supplementary Figs. S2, S3).

3.1. SKS and SKKS waveforms

It is visually apparent that for a swath of the azimuths between $\sim 25\text{--}43^\circ$ and for distances between $\sim 110\text{--}119^\circ$, a coherent SKKS arrival can be observed on the transverse components (indicating splitting) for both events. The seismograms, bandpass-filtered between 8 and 25 s, for this distance and azimuth range are shown in Fig. 3 (event 1) and S4 (event 2). In contrast, the corresponding SKS phase does not show a coherent splitting signal, despite

similar noise levels for both phases. The raypaths of the apparently split SKKS phases sample the lowermost mantle in region A shown in Fig. 1a.

While substantial SKS-SKKS splitting discrepancies are typically interpreted as reflecting a contribution from lowermost mantle anisotropy, it is important to rule out possible contributions from the upper mantle. Previous work has shown that for particular anisotropic geometries sampled over specific backazimuths, modest SKS-SKKS splitting discrepancies can be caused by upper mantle anisotropy (Tesoniero et al., 2020; Wolf et al., 2022a). In this case, however, we observe the discrepant signal (that is, strong, coherent splitting of SKKS phases vs. incoherent splitting of SKS phases) across a large region of highly variable upper mantle anisotropy for both events (Fig. 1b). Therefore, splitting due to upper mantle anisotropy can be excluded as a plausible explanation for the observations. In order to substantiate this inference, we carry out global wavefield simulations using AxiSEM3D (Leng et al., 2016, 2019) for a global model that includes realistic azimuthal anisotropy beneath the western US stations (Zhu et al., 2020) and show that coherent SKS-SKKS splitting discrepancies are not pre-

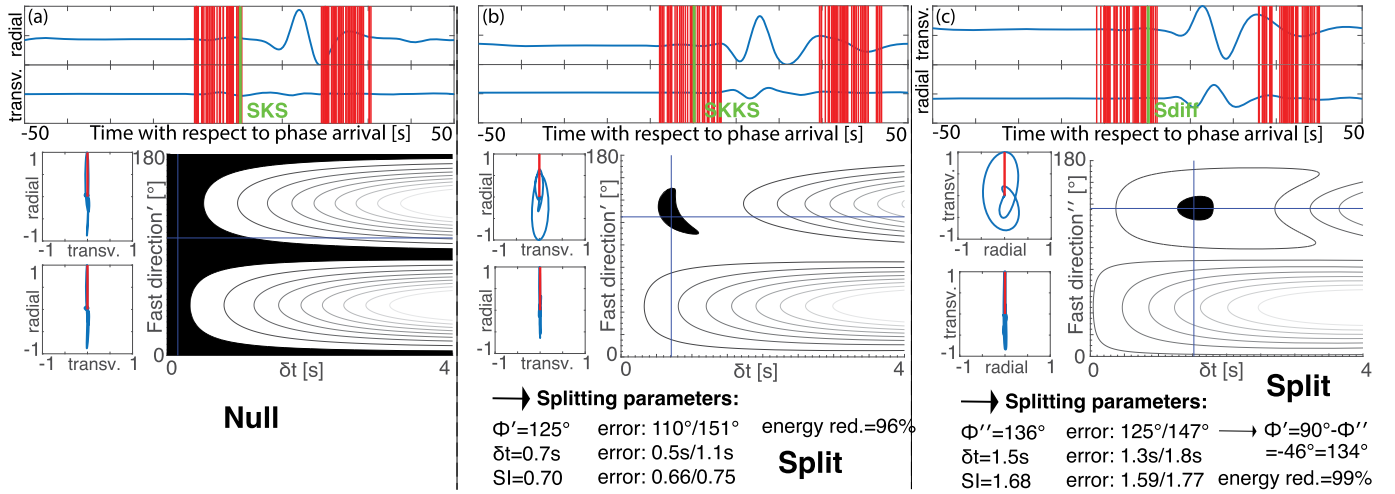


Fig. 4. Splitting diagnostic plots from SplitRacer (Reiss and Rumpker, 2017) for the stacked waveforms from Fig. 3. (a) The top row shows the waveforms of the SKS stack (radial, top trace; transverse, bottom trace) as blue solid line, the predicted arrival SKS arrival as a green line and the start/end of the 50 randomly chosen measurement windows with red lines. The upper diagram to the left shows the particle motion for the original stack, the lower diagrams for the waveforms that were corrected for splitting. The red lines in the diagrams indicate the backazimuthal direction. The best fitting splitting parameters are shown in the $\phi' - \delta t$ -plane, with black color indicating the 95% confidence region. The stacked SKS waveforms are not split (null). ϕ' is calculated in a ray-attached coordinate frame, meaning that the traditional fast direction ϕ (in a station centered coordinate frame, measured from geographic north) and ϕ' are identical if the radial component is aligned with the north direction. (b) Same representation as in panel (a), but for the SKKS phase. The SKKS is clearly split. (c) Same representation as in panel (a) but here for the S_{diff} phase (transverse component is shown on top; radial component at bottom trace, in waveform traces). S_{diff} is the phase that experiences the strongest splitting.

dicted (discussed further in Section 4 below). We infer, therefore, that the coherently split SKKS phases sample a region of uniform lowermost mantle anisotropy, while the corresponding SKS phases are not generally affected by D'' anisotropy (they either sample an effectively isotropic region, or they sample D'' anisotropy in a geometry that does not cause substantial splitting of the waveforms). We do not observe discrepant SKS-SKKS splitting for waveform pairs that sample region B (Fig. 1b), likely because SKS and SKKS both sample similar lowermost mantle anisotropy. We also identify region C (Fig. 1b), for which no SKS-SKKS differential splitting can be observed.

3.2. S_{diff} waveforms

Visual inspection of the S_{diff} phases from event 1 (Fig. 2) reveals that they also exhibit splitting, with substantial radial component energy observed on the seismograms in the azimuth range $28-43^\circ$ and the distance range $112-120^\circ$ (Fig. 3). This azimuth range is identical to that for which differential SKS-SKKS splitting is observed (Fig. 1b). Fig. 1d shows the portions of the split S_{diff} raypaths that sample the D'' layer (region D in Fig. 1d). We also identify region E (Fig. 1d), for which S_{diff} is not clearly split; for these paths, there is no indication of lowermost mantle anisotropy being present.

While S_{diff} has often been used to interrogate anisotropy at the base of the mantle (e.g., Vinnik et al., 1989), several challenges with S_{diff} splitting measurements have been pointed out. In particular, it has been shown that the assumption that SV_{diff} has died off at any particular distance does not always hold; further, even for isotropic models, a time lag between the SH and SV portions of S_{diff} can be accumulated, which could potentially mimic splitting (Komatitsch et al., 2010; Borgeaud et al., 2016). In the past, this challenge has been addressed by arguing that in absence of seismic anisotropy, only a negligible SV_{diff} component could be expected of the waves under study (Cottaar and Romanowicz, 2013). We use a similar strategy to determine whether the S_{diff} data for events 1 and 2 can be used to measure lowermost mantle anisotropy by running simulations for realistic isotropic deep mantle velocity structure for our study region. We calculate synthetics for both events for the stations in the distance and azimuth range

of interest. The initial input model that we use for these synthetics is isotropic PREM (Dziewonski and Anderson, 1981), which we then replace with the regional (isotropic) tomography model from Suzuki et al. (2021) for the lowermost mantle. We additionally incorporate ultra-low velocity zones at the base of the mantle at the positions that are reported in database from Yu and Garnero (2018). The characteristics assumed for these low velocity anomalies are a thickness of 20 km, a 20% reduction in S wave velocity, and a 10% reduction in P wave velocity (with respect to PREM). The corresponding synthetics show little or arriving SV energy for event 1 and clearly discernible SV energy for event 2 (Fig. S1).

This result implies that in the absence of anisotropy, the S_{diff} phases for this event-stations geometry should be almost perfectly SH-polarized for event 1. Further, for event 1, there is no recognizable and coherent SV energy for distances between 107° and 110° (Fig. 2), indicating that any initial SV-polarized energy portion of the wave has died off (as expected for increasing distances from the source). For distances larger than 112° , however, the SV energy associated with the S_{diff} arrival increases dramatically (Fig. 2); we interpret this energy as reflecting splitting due to lowermost mantle anisotropy. This SV energy is coherent between 112° and 120° epicentral distance. Furthermore, it does not accumulate an observable time shift with respect to the SH component of S_{diff} for distances larger than 112° ; neither does it exhibit any unusual waveform effects. This convinces us that the observed signal is, indeed, due to D'' anisotropy. In contrast to event 1, event 2 shows SV energy in the (isotropic) synthetic simulations and does not show such an absence of SV energy for any particular distance interval, such that we cannot confidently exclude an effect of initial SV energy on the waveforms, and we cannot confidently attribute the radial component energy to the effect of splitting. This is why we only analyze SKS and SKKS phases for event 2, and we do not attempt to measure S_{diff} splitting for this event.

A further potential complication in the interpretation of S_{diff} waveforms is possible phase interference at these distances, for example through depth phases (Parisi et al., 2018), which can potentially interfere with S_{diff} splitting measurements. In order to rule out this effect, we calculate ray-theoretical travel times for depth phases to make sure that no significant interaction of other phases with S_{diff} can be expected in the distance interval under

study. Additionally, our calculated synthetics for S_{diff} for event 1 do not show evidence for phase interactions with any exotic phases (e.g., Figs. 2 and 3).

3.3. Shear wave splitting measurements

After conducting this first visual and qualitative analysis, we focus on those data that reflect the influence of D'' anisotropy (raypaths sampling regions A and D; red color in Fig. 1a and d), with waveforms shown in Fig. 3 (event 1) and Fig. S5 (event 2). For each phase of interest (SKS, SKKS and S_{diff}), we normalize all traces (with respect to the maximum amplitude of the radial component for SK(K)S and the transverse for S_{diff}), align them via cross-correlation, and linearly stack them. As anticipated from our visual inspection, we find that the stacked transverse component of SKS, recorded across the region shown in Fig. 1b, does not show a coherent signal (Fig. 3, S5); in contrast, an arrival is clearly visible on the transverse component of the SKKS stack. The same is true for the radial component of S_{diff} (Fig. 3). The stacked transverse component of the SKKS phase has the shape of the time derivative of the radial component, as predicted for waveforms that have undergone shear wave splitting; similarly, the radial component of S_{diff} has the shape of the time derivative of the transverse component. The S_{diff} phase seems to exhibit stronger splitting than the SKKS phase, based on the relative amplitudes of the horizontal components. Example waveforms for a candidate event that was not retained in our analysis, although its raypaths are similar to those from events 1 and 2, are shown in Fig. S6 (see Table S1 for event information). The lower signal-to-noise ratio for this event prevents the visual detection of SKS-SKKS differential splitting, although the final stack shows that SKKS is more split than SKS. However, the influence of the noise on the stacked waveform is hard to quantify, which is why we focus our splitting analysis on events 1 and 2.

We conduct shear-wave splitting analysis (Silver and Chan, 1991; Chevrot, 2000) on the stacked data (SKS and SKKS phases for both events, and S_{diff} for event 1). While the stacked SKS phases do not show splitting (Fig. 4a, S6a), the stacked SKKS splitting parameters ($\phi' = 125^\circ$ and 128° and $\delta t = 0.7$ s and 1.0 s, and $SI = 0.7$ and 0.85) are similar for both events. The absence of splitting for the SKS stacks indicates that the upper mantle splitting signal is not coherent across the stacked seismograms and that transverse component energy cancels out in the stacks; in contrast, the coherent SKKS splitting can be attributed to lowermost mantle anisotropy (S8-S9). A similar argument can be made for the stacked S_{diff} arrival for Event 1, which yields well-constrained splitting parameters ($\phi' = 134^\circ$, $\delta t = 1.5$ s, and $SI = 1.68$). The difference in splitting parameters between SKKS and S_{diff} , particularly δt and SI , is not unexpected, given the differences in lowermost mantle path length, propagation direction, and initial polarization between the phases.

Although we do not interpret S_{diff} splitting for event 2 because we cannot exclude the possibility that initial SV_{diff} energy is influencing our measurements (see Section 3.2), we still measure the corresponding splitting parameters (Fig. S7). Interestingly, the S_{diff} splitting parameters for event 2 are almost identical to those from event 1, likely indicating that both events sample similar lowermost mantle anisotropy.

We emphasize that a stacking approach across such a large region is only justified because the individual seismograms are split similarly. While this is visually apparent in Fig. 3, we also conduct a shear wave splitting analysis of the individual seismograms from event 1 to confirm this impression. The well-constrained single station SKKS and S_{diff} splitting parameters obtained in this analysis are shown in Supplementary Fig. S9. While these individual measurements may be influenced by upper mantle anisotropy,

the lowermost mantle contribution is apparently strong enough that generally consistent splitting parameters can be observed over the whole distance and azimuth range (although upper mantle anisotropy is variable; see Fig. 1b), thus providing a further confirmation for the validity of the stacking approach.

4. Forward modeling results

To test our hypothesis that the absence of splitting for the SKS stacks indicates that the upper mantle splitting signal is not coherent across the stacked seismograms (and effectively cancels out in the stacks), we conduct full-wave simulations using AxisEM3D (Leng et al., 2016, 2019). We calculate synthetic seismograms for event 1, incorporating the azimuthal anisotropy model US32 (Zhu et al., 2020) in our modeling (as described in Section 2.2) with PREM (Dziewonski and Anderson, 1981) as our background model. We then add a realistic level of Gaussian noise to our synthetics (attempting to visually match the noise level of the real data) and apply the same stacking process to the synthetics as for the real data (Fig. S8). We find that the stacked synthetic SKS and SKKS stacks have essentially no transverse component energy, showing that realistic upper mantle anisotropy does not generate a coherent difference in SKS and SKKS splitting across the array.

While the comparison between the synthetic stacked SKS and SKKS phases and the observed stacked waveforms is instructive, we also carry out splitting measurements on individual (synthetic and actual) waveforms in order to understand the effect of upper mantle anisotropy on our data set. We measure splitting intensity for individual waveforms for event 1, both for the actual data and for the synthetic waveforms generated for upper mantle anisotropy model US32. In Fig. 5, we show single-station splitting intensity measurements for the real and synthetic data. This comparison shows that while US32 predicts an accurate splitting strength for our region of interest, its details do not perfectly match the real data. This is not unsurprising, considering that US32 was derived from surface wave data and not directly from SKS splitting measurements. Comparing SKS and SKKS splitting for the real data (left column), we see that the SKKS phases are consistently more strongly split than SKS, while SKS and SKKS phases are split similarly for the synthetic data (left column). This observation confirms our observation from Fig. 2 that SKKS is more strongly split than SKS; additionally, the fact that discrepant SKS-SKKS splitting cannot be reproduced with upper mantle anisotropy further strengthens our inference that the strong SKKS splitting is indeed caused by lowermost mantle anisotropy.

Given our finding that the stacked splitting parameters for SKKS and S_{diff} reflect splitting due to lowermost mantle anisotropy, we next carry out a series of forward modeling experiments using AxisEM3D (Leng et al., 2016, 2019) to simulate global wave propagation through a model that includes lowermost mantle anisotropy. Because the lowermost mantle beneath the northeastern Pacific is likely dominated by slab remnants, implying lower than average temperatures and a relatively shallow bridgmanite-postperovskite transition (Murakami et al., 2004), Asplet et al. (2020) suggested that lattice-preferred orientation (LPO) of post-perovskite (Ppv) (Stackhouse et al., 2005; Wookey et al., 2005b; Wentzcovitch et al., 2006) is most likely mechanism for anisotropy in this region. Our main focus is therefore modeling Ppv anisotropy at the base of the mantle, but we also run simulations for bridgmanite (Br) and ferropericlase (Fp) mineralogies. We do not simulate shape-preferred orientation because partial melt is unlikely to be present in a region of fast velocities at the base of the mantle.

We model a variety of plausible lowermost mantle elastic tensors from a previously published elastic tensor library (Creasy et al., 2020) in our simulations, assuming a simple shear deformation geometry, a horizontal shear direction (Kendall and Silver, 1996),

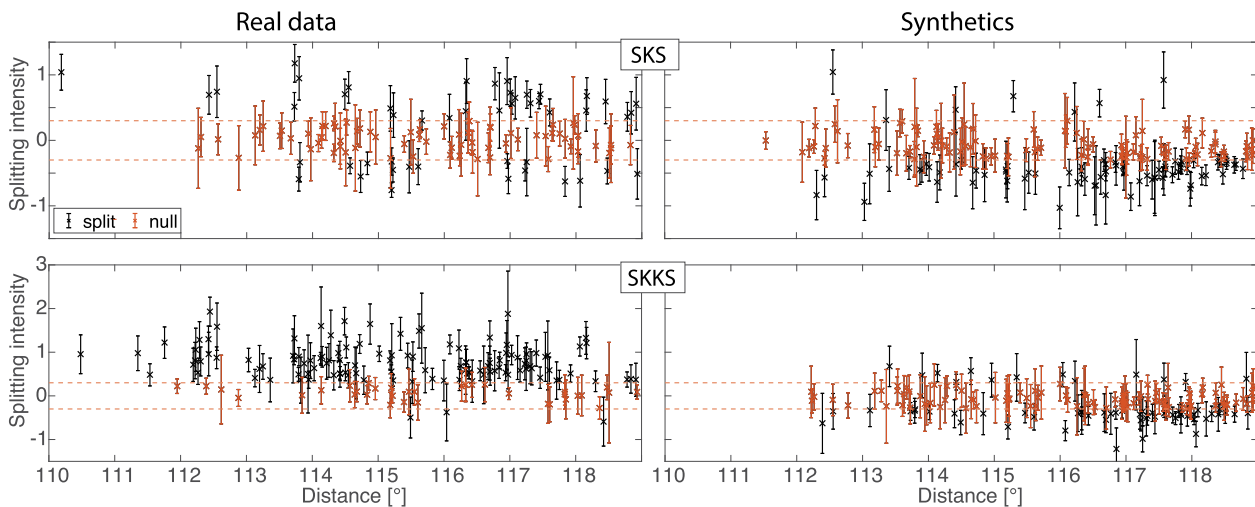


Fig. 5. SKS (upper row) and SKKS (lower row) splitting intensity measurements for individual waveforms for actual data (left column) and synthetic data (right column). The synthetics (shown in Fig. S9) were run for the azimuthally anisotropic model US32 (Zhu et al., 2020), which includes the depth range 0 to 1000 km. Red dashed lines are plotted at splitting intensity values of -0.3 and 0.3 . Null measurements (defined as $0.3 > |SI|$) are plotted in red, all other values are shown in black. Error bars indicate 95% confidence intervals. Low quality measurements were discarded and are not presented here. A measurement is defined as ‘low quality’ if 1. it is unclear whether splitting or noise is measured, 2. the transverse looks unlike the time derivative of the radial or 3. the 95% confidence interval is larger than ± 0.5 , although for some large splitting intensity values larger 95% confidence intervals were accepted (the larger the splitting intensity, the larger the absolute value uncertainties tend to be).

and a shear strain of $\gamma = 1$, or 100% strain. We consider a variety of potential shear directions by rotating the candidate elastic tensors in steps of 10° in the horizontal plane. The tensors we use are based on single crystal elasticity predicted by four different studies (Karki et al., 1999, for Fp; Wookey et al., 2005b, for Br; Stackhouse et al., 2005, and Wentzcovitch et al., 2006, for Ppv). The Ppv anisotropy scenarios were modeled assuming three different candidate dominant slip systems ($[100](010)$, $[100](001)$ and $\{011\}\langle 0-11 \rangle + \{010\}\langle 100 \rangle$ slip); the Br scenarios were modeled for a dominant $(100)\langle 010 \rangle + (100)\langle 011 \rangle$ and (011) slip systems. For the Fp simulations, dominant $\{100\}\langle 011 \rangle$ and $\{110\}\langle 1-10 \rangle$ slip was assumed (Creasy et al., 2020). Unless stated otherwise, the thickness of the anisotropic layer that we incorporate is 300 km. We use isotropic PREM (Dziewonski and Anderson, 1981) in all other regions. We assume PREM-like density structure in the lowermost mantle and do not change the elastic tensor as a function of depth, which leads to a slightly negative velocity gradient at the base of the mantle.

We first model splitting of the SKKS phases at one representative station (Fig. 1b) for all possible horizontal shear directions for the six candidate Ppv elastic tensors (Figs. S11–S16) and the four Br and Fp elastic tensors (S17); an example of this modeling is shown in Fig. 6. We find that all six Ppv tensors show similar splitting patterns (ϕ , δt , SI) as a function of shear direction, which implies that the interpretation in terms of plausible flow geometries does not depend strongly on the choice of dominant slip system and single-crystal elastic constants. We find that three out of the six Ppv tensors do not predict sufficiently strong splitting for a 300 km thick anisotropic layer (S11a,b; S12b), which is a reasonable maximum thickness to assume for Ppv at the base of the mantle in our study region (Suzuki et al., 2021). We therefore focus our subsequent modeling on the three remaining tensors. Based on our initial model results, we define a swath of plausible shear directions that are potentially consistent with the SKKS fast splitting directions (pink regions in Figs. S10–S12), and focus on this subset of models in our second set of simulations. For these candidate directions, we repeat our simulations, applying the precise stacking workflow as for the real data and adjusting the thickness of the anisotropic layer to match the splitting strength (as expressed in the SI and δt measurements). We also test whether the anisotropic models that can match the stacked SKKS splitting

observations are also capable of matching the stacked S_{diff} splitting observations. The splitting results from the stacked synthetics for the three Ppv models are presented in Fig. 6 (which shows Ppv with a dominant $[100](010)$ slip system) and supplementary Figs. S13–S15 (which show results for all slip systems, all generally similar to those shown in Fig. 6). These models demonstrate that the S_{diff} splitting results can be reproduced with the same deformation geometry that successfully matches the SKKS splitting results. A plausible scenario, then, is that the lowermost mantle beneath the entire northeastern Pacific Ocean (regions D, B, and A in Fig. 1) is dominated by a coherent, uniform region of anisotropy that results from lowermost mantle flow. Furthermore, our models suggest a shear direction oriented roughly to the south (or, equivalently, north), consistent with southwards – or northwards – directed flow at the base of the mantle.

Results for another set of simulations for tensors representing Br and Fp anisotropy are shown in Fig. S17. We find that for some shear direction azimuths, Br anisotropy can also simultaneously explain the observed SKKS and S_{diff} splitting measurements. Interestingly, under the assumption of simple horizontal shear deformation, the shear direction azimuths that can explain that can explain the real data measurements for Br are very similar to those inferred for Ppv, and thus also consistent with dominant north- or south-directed flow (Fig. S17). On the other hand, none of the Fp scenarios can simultaneously explain the SKKS and S_{diff} splitting measurements (Fig. S17).

The anisotropic region found in this study is spatially coincident with a relatively strongly anisotropic region mapped by Suzuki et al. (2021), extending between 100–200 km above the core-mantle boundary. However, it is not entirely clear how far our mapped anisotropic region extends to the east and west, so the geographic overlap may not be perfect. Our observation that the SKS phases that sample the lowermost mantle in region A are not influenced by lowermost mantle anisotropy may be due to the absence of seismic anisotropy in the region sampled by SKS. Alternatively, the anisotropic region could extend to the east and be sampled by SKS, but due to the difference in incidence angle between SKS and SKKS phases, SKS would not be split. To explore this possibility, we also measure SKS splitting for the suggested plausible anisotropy scenarios; these results are shown in Fig. S18. Furthermore, we find that for some scenarios, our models indeed

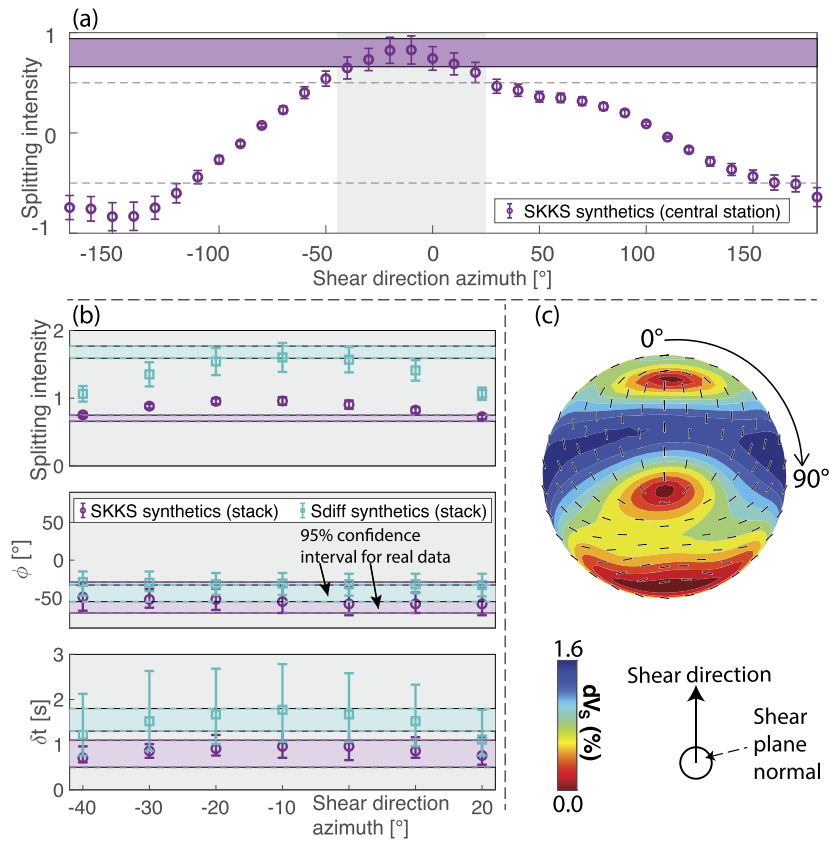


Fig. 6. Comparison of observations and model results for a Ppv tensor with a dominant slip of [100](010). (a) Splitting intensity (measured for one representative central station, see Fig. 1a) as a function of elastic tensor rotation angle (=shear direction azimuth), in degrees from North. The synthetic seismograms were analyzed precisely as the real data, shown in Figs. 3 and 4, using the same elastic tensor as for Figs. S10b and S13. Error bars represent 95% confidence intervals. Violet shaded colors indicate the 95% confidence regions of the splitting parameters measured on the real data stacks for SKKS. Light gray shading indicates the range of shear direction azimuths that could potentially explain the observations. (b) Predictions and observations of SKKS (violet) and S_{diff} (blue) splitting intensity (top row), ϕ' and δt (bottom row) as a function of shear direction. Symbols show splitting parameters for stacked synthetic seismograms for event 1, generated for a model with a 250 km thick Ppv layer at the base of the mantle, plotted as a function of shear direction. Only successful models are shown. Shaded colors (SKKS: violet; S_{diff} : blue) indicate the 95% confidence regions of the splitting parameters measured on the real data stacks. Other plotting conventions are similar to panel a. (c) Upper hemisphere representation of the elastic tensor used in simulation to represent anisotropy in D'' , plotted with MSAT (Walker and Wookey, 2012). Black sticks represent fast S polarization directions. The shear plane is oriented horizontally and the tensor is rotated clockwise in the horizontal plane to test different candidate shear directions.

predict weak or absent SKS splitting in cases in which the corresponding SKKS phase is split. However, this depends on the details of the elasticity tensor and the sampling direction, so we cannot distinguish with confidence the cause of the lack of SKS splitting in region A.

Overall, we hypothesize that both phases (SKS and SKKS) that sample the lowermost mantle in region B are split similarly by D'' anisotropy, which leads to non-discrepant splitting. This is also suggested by the spatial distribution shown in Fig. 1a. However, we cannot exclude the possibility that SKS and SKKS are also differentially split by D'' anisotropy for region B. Such a discrepant splitting signature could then have been obscured by the relatively strong upper mantle anisotropy beneath the stations where the corresponding seismograms were recorded. Moreover, we prefer the scenario in which SKS does not sample lowermost mantle anisotropy over the scenario in which the lack of SKS splitting is explained by the difference in incidence angle, because the latter scenario requires quite specific sampling azimuths of the anisotropy (Fig. S18).

Based on our modeling results, then, we propose the following scenario. We suggest that our observations are best explained by a region of anisotropy dominated by LPO of Ppv formed by horizontal shearing just above the core-mantle boundary. Our modeling constrains the direction of horizontal shearing to be approximately southward (or, equivalently, northward). We infer that this

anisotropic geometry dominates throughout the entire northeastern Pacific Ocean region.

5. Geodynamic implications

Fig. 7 provides a schematic illustration of a possible set of geodynamic processes and deformation geometry in the lowermost mantle beneath the northeastern Pacific would be consistent with our measurements. Given the long history of subduction beneath the northern Pacific Ocean (for at least the past 250 million years (e.g., Matthews et al., 2016; Merdith et al., 2021), and considering a transit time of slabs to the CMB of approximately 240 million years (Le Pichon et al., 2019), it is highly likely that slab material is currently piling up above the CMB, displacing existing mantle and driving lowermost mantle flow (Fig. 7). Beneath our study region, we suggest that relict slabs impinging on the CMB may be pushing material to the south (at higher latitudes, it is likely that slabs are driving flow to the north; see Fig. 7c,d), inducing LPO of Ppv through horizontal shearing. That a coherent signal of lowermost mantle anisotropy is observable across a large set of seismic stations suggests that the flow extends across a large area in the lowermost mantle, having at least the size of region A in Fig. 1a.

We have combined seismic observations across a dense, large-aperture seismic array with detailed computational modeling informed by mineral physics constraints to resolve lowermost mantle anisotropy beneath our study region. Using a set of reasonable

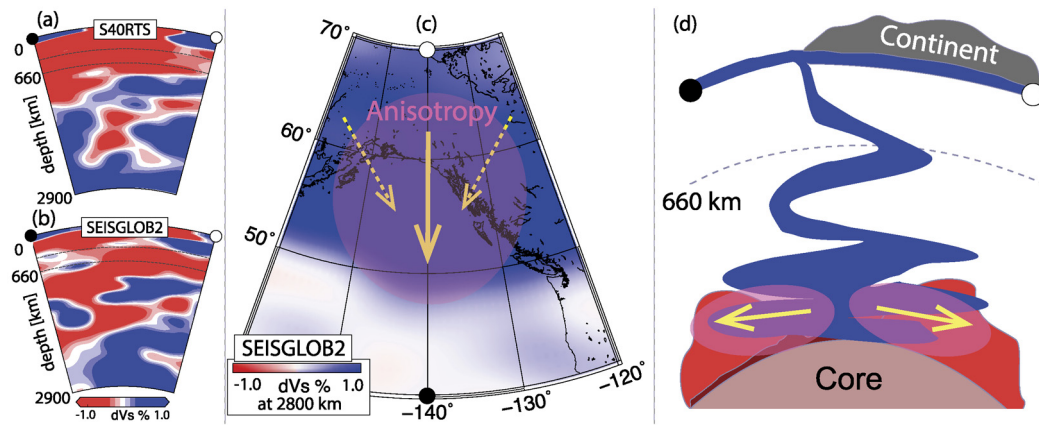


Fig. 7. Schematic representation of our preferred flow scenario. (a) Tomographic cross-section of S-wave velocity perturbations along longitude 140° west for model S40RTS (Ritsema et al., 2011), visualized using Submachine (Hosseini et al., 2018). (b) Like (a) for the tomographic model SEISGLOB2 (Durand et al., 2017). (c) Map view of the anisotropic region (pink). Background colors show velocity perturbations with respect to PREM (Dziewonski and Anderson, 1981) at 2800 km depth according to SEISGLOB2. Yellow arrows indicate the range of permissible directions of material flow (\sim north-south) consistent with our observations. (d) Our interpretation of the processes leading to north-south flow: Subducting slabs (blue) pile up in the lower mantle, displacing hotter material (red) or slab material that has been subducted earlier, thus invoking north-south flow (arrows) and patches of seismic anisotropy (pink).

assumptions, these tools allow us to infer a plausible lowermost mantle flow direction for the northeastern Pacific Ocean and propose a connection with relict subducting slabs. Such a combination of methods can be applied to other datasets going forward, allowing us to make specific quantitative inferences of flow geometries at the base of the mantle. Specifically, the approach we have implemented here avoids some of the restrictive assumptions that were made by previous work that inferred flow at the base of the mantle, such as reliance on ray theory or on single crystal elastic tensors (e.g., Wolf et al., 2019; Creasy et al., 2021).

We can compare our inference of south- (or perhaps north-) directed mantle flow with predictions from previous global models of flow and anisotropy. Specifically, Walker et al. (2011) suggested eastward flow for the northern part of our study area, with the southern part dominated by southeastward flow, while the results of Flament (2018) suggest northeastward flow in the northern part and generally eastward flow in the southern part. Interestingly, neither of these flow model predictions is particularly consistent with our observational results, which suggest flow to the south. The reason for this difference, and for the differences between the predictions of the different models, is not entirely clear. We note, however, that a number of assumptions must be made in order to generate predictions of large-scale mantle flow, including mantle rheology and the relative importance of thermal vs. chemical contributions to density perturbations. Furthermore, some modeling approaches explicitly account for surface plate motions and the history of subduction (e.g., Flament, 2018), while others rely on density perturbations inferred from seismic tomography to drive flow. An observational and modeling approach like ours to measuring and interpreting seismic anisotropy can help validate model predictions and potentially improve different approaches to predicting patterns of lowermost mantle flow.

6. Summary

Our investigation of SKS, SKKS, and S_{diff} waveforms in North America that sample the base of the mantle beneath the northeastern Pacific Ocean yields evidence for strong, coherent splitting due to seismic anisotropy in the lowermost mantle. The strong splitting signal due to this anisotropy can be observed across a large swath of USArray stations, indicating a relatively large size of this uniformly isotropic region in the lowermost mantle and allows us to make particularly robust estimates of the shear wave splitting parameters. Simulations of the global seismic wavefield

for models that include realistic anisotropy scenarios for LPO of Ppv reveals evidence for flow in a southwards (or, equivalently, northwards) direction at the base of the mantle. Such a flow field can be explained by subducted slab material impinging on the core-mantle boundary, pushing material to the south beneath our study area. The combination of tools applied in this work holds promise to substantially improve the resolution of lowermost mantle anisotropy. Comparisons between observations of D'' anisotropy and predictions from global flow models will improve our understanding of the patterns and drivers of lowermost mantle flow.

Data availability

All USArray (IRIS Transportable Array, 2003) data were downloaded through IRIS (<https://service.iris.edu/>). Synthetic seismograms for this study were computed using AxiSEM3D, which is publicly available at <https://github.com/AxiSEMunity/AxiSEM3D>.

CRediT authorship contribution statement

JW and MDL developed this project together; JW wrote the codes and analyzed the data; JW and MDL contributed to writing the manuscript; JW created the figures for the manuscript.

Declaration of competing interest

The authors declare that they have no known competing financial interests or personal relationships that could have appeared to influence the work reported in this paper.

Acknowledgements

This work was funded by Yale University and grant EAR-1547499 to MDL. We thank the Yale Center for Research Computing for providing the necessary HPC infrastructure. The Generic Mapping Tools (Wessel and Smith, 1998), ObsPy (Beyreuther et al., 2010), MSAT (Walker and Wookey, 2012) and SplitRacer (Reiss and Rumpker, 2017) were used in this research. We are grateful to Sanne Cottaar and an anonymous reviewer for their constructive comments that helped us improve the manuscript.

Appendix A. Supplementary material

Supplementary material related to this article can be found online at <https://doi.org/10.1016/j.epsl.2022.117758>.

References

- Asplet, J., Wookey, J., Kendall, M., 2020. A potential post-perovskite province in D'' beneath the Eastern Pacific: evidence from new analysis of discrepant SKS-SKKS shear-wave splitting. *Geophys. J. Int.* 221, 2075–2090. <https://doi.org/10.1093/gji/ggaa114>.
- Barruol, G., Kern, H., 1996. Seismic anisotropy and shear-wave splitting in lower-crustal and upper-mantle rocks from the Ivrea Zone: experimental and calculated data. *Phys. Earth Planet. Inter.* 95, 175–194. [https://doi.org/10.1016/0031-9201\(95\)03124-3](https://doi.org/10.1016/0031-9201(95)03124-3).
- Beyreuther, M., Barsch, R., Krischer, L., Megies, T., Behr, Y., Wassermann, J., 2010. Obspy: a python toolbox for seismology. *Seismol. Res. Lett.* 81, 530–533. <https://doi.org/10.1111/10.1785/gssrl.81.3.530>.
- Borgeaud, A.F., Konishi, K., Kawai, K., Geller, R.J., 2016. Finite frequency effects on apparent S-wave splitting in the D'' layer: comparison between ray theory and full-wave synthetics. *Geophys. J. Int.* 207, 12–28. <https://doi.org/10.1093/gji/ggw254>.
- Chang, S.J., Ferreira, A.M., Ritsema, J., van Heijst, H.J., Woodhouse, J.H., 2014. Global radially anisotropic mantle structure from multiple datasets: a review, current challenges, and outlook. *Tectonophysics* 617, 1–19. <https://doi.org/10.1016/j.tecto.2014.01.033>.
- Chevrot, S., 2000. Multichannel analysis of shear wave splitting. *J. Geophys. Res., Solid Earth* 105, 21579–21590. <https://doi.org/10.1029/2000JB900199>.
- Cottaar, S., Romanowicz, B., 2013. Observations of changing anisotropy across the southern margin of the African LLSVP. *Geophys. J. Int.* 195, 1184–1195. <https://doi.org/10.1093/gji/ggt285>.
- Creasy, N., Miyagi, L., Long, M.D., 2020. A library of elastic tensors for lowermost mantle seismic anisotropy studies and comparison with seismic observations. *Geochem. Geophys. Geosyst.* 21, e2019GC008883. <https://doi.org/10.1029/2019GC008883>.
- Creasy, N., Pisconti, A., Long, M.D., Thomas, C., 2021. Modeling of seismic anisotropy observations reveals plausible lowermost mantle flow directions beneath Siberia. *Geochem. Geophys. Geosyst.*, e2021GC009924. <https://doi.org/10.1029/2021GC009924>.
- Durand, S., Debayle, E., Ricard, Y., Zanolli, C., Lambotte, S., 2017. Confirmation of a change in the global shear velocity pattern at around 1000 km depth. *Geophys. J. Int.* 211, 1628–1639. <https://doi.org/10.1093/gji/ggx405>.
- Dziewonski, A.M., Anderson, D.L., 1981. Preliminary reference Earth model. *Phys. Earth Planet. Inter.* 25, 297–356. [https://doi.org/10.1016/0031-9201\(81\)90046-7](https://doi.org/10.1016/0031-9201(81)90046-7).
- Flament, N., 2018. Present-day dynamic topography and lower-mantle structure from palaeogeographically constrained mantle flow models. *Geophys. J. Int.* 216, 2158–2182. <https://doi.org/10.1093/gji/ggy526>.
- French, S.W., Romanowicz, B.A., 2014. Whole-mantle radially anisotropic shear velocity structure from spectral-element waveform tomography. *Geophys. J. Int.* 199, 1303–1327. <https://doi.org/10.1093/gji/ggu334>.
- van der Hilst, R., Widiyantoro, S., Engdahl, E., 1997. Evidence for deep mantle circulation from global tomography. *Nature* 386, 578–584. <https://doi.org/10.1038/386578a0>.
- Hosseini, K., Matthews, K.J., Sigloch, K., Shephard, G.E., Domeier, M., Tsekhmistrenko, M., 2018. SubMachine: web-based tools for exploring seismic tomography and other models of Earth's deep interior. *Geochem. Geophys. Geosyst.* 19, 1464–1483. <https://doi.org/10.1029/2018GC007431>.
- IRIS Transportable Array, 2003. USArray Transportable Array. <https://www.fdsn.org/networks/detail/TA/10.7914/SN/TA>.
- Karki, B.B., Wentzcovitch, R.M., de Gironcoli, S., Baroni, S., 1999. First-principles determination of elastic anisotropy and wave velocities of MgO at lower mantle conditions. *Science* 286, 1705–1707. <https://doi.org/10.1126/science.287.5450.41f>.
- Kendall, J.M., Silver, P., 1996. Constraints from seismic anisotropy on the nature of the lower mantle. *Nature* 381, 409–412. <https://doi.org/10.1038/381409a0>.
- Komatitsch, D., Vinnik, L.P., Chevrot, S., 2010. Shdiff-svdiff splitting in an isotropic Earth. *J. Geophys. Res., Solid Earth* 115. <https://doi.org/10.1029/2009JB006795>.
- Kustowski, B., Ekström, G., Dziewoński, A.M., 2008. Anisotropic shear-wave velocity structure of the Earth's mantle: a global model. *J. Geophys. Res., Solid Earth* 113, B06306. <https://doi.org/10.1029/2007JB005169>.
- Le Pichon, X., Sengör, A.M.C., Imren, C., 2019. Pangea and the lower mantle. *Tectonics* 38, 3479–3504. <https://doi.org/10.1029/2018TC005445>.
- Leng, K., Nissen-Meyer, T., van Driel, M., 2016. Efficient global wave propagation adapted to 3-D structural complexity: a pseudospectral/spectral-element approach. *Geophys. J. Int.* 207, 1700–1721. <https://doi.org/10.1093/gji/ggw363>.
- Leng, K., Nissen-Meyer, T., van Driel, M., Hosseini, K., Al-Attar, D., 2019. AxisEM3D: broad-band seismic wavefields in 3-D global Earth models with undulating discontinuities. *Geophys. J. Int.* 217, 2125–2146. <https://doi.org/10.1093/gji/ggz092>.
- Lithgow-Bertelloni, C., Richards, M.A., 1998. The dynamics of Cenozoic and Mesozoic plate motions. *Rev. Geophys.* 36, 27–78. <https://doi.org/10.1029/97RG02282>.
- Liu, K., Elsheikh, A., Lemnifi, A., Purevsuren, U., Ray, M., Refayee, H., Yang, B., Yu, Y., Gao, S., 2014. A uniform database of teleseismic shear wave splitting measurements for the western and central United States. *Geochem. Geophys. Geosyst.* 15, 2075–2085. <https://doi.org/10.1002/2014GC005267>.
- Long, M., 2009. Complex anisotropy in D'' beneath the eastern Pacific from SKS-SKKS splitting discrepancies. *Earth Planet. Sci. Lett.* 283, 181–189. <https://doi.org/10.1016/j.epsl.2009.04.019>.
- Long, M.D., Becker, T., 2010. Mantle dynamics and seismic anisotropy. *Earth Planet. Sci. Lett.* 297, 341–354. <https://doi.org/10.1016/j.epsl.2010.06.036>.
- Matthews, K., Maloney, K., Zahirovic, S., Williams, S., Seton, M., Müller, D., 2016. Global plate boundary evolution and kinematics since the late Paleozoic. *Glob. Planet. Change* 146, 226–250. <https://doi.org/10.1016/j.gloplacha.2016.10.002>.
- Merdith, A.S., Williams, S.E., Collins, A.S., Tetley, M.G., Mulder, J.A., Blades, M.L., Young, A., Armistead, S.E., Cannon, J., Zahirovic, S., Müller, R.D., 2021. Extending full-plate tectonic models into deep time: linking the Neoproterozoic and the Phanerozoic. *Earth-Sci. Rev.* 2021, 103477. <https://doi.org/10.1016/j.earscirev.2020.103477>.
- Murakami, M., Hirose, K., Kawamura, K., Sata, N., Ohishi, Y., 2004. Post-perovskite phase transition in MgSiO₃. *Science* 304, 855–858. <https://doi.org/10.1126/science.1095932>.
- Nowacki, A., Wookey, J., Kendall, J.M., 2010. Deformation of the lowermost mantle from seismic anisotropy. *Nature* 467, 1091–1094. <https://doi.org/10.1038/nature09507>.
- Panning, M., Romanowicz, B., 2006. A three-dimensional radially anisotropic model of shear velocity in the whole mantle. *Geophys. J. Int.* 167, 361–379. <https://doi.org/10.1111/j.1365-246X.2006.03100.x>.
- Parisi, L., Ferreira, A.M.G., Ritsema, J., 2018. Apparent splitting of s waves propagating through an isotropic lowermost mantle. *J. Geophys. Res., Solid Earth* 123, 3909–3922. <https://doi.org/10.1002/2017JB014394>.
- Reiss, M., Rümpler, G., 2017. SplitRacer: MATLAB code and GUI for semiautomated analysis and interpretation of teleseismic shear-wave splitting. *Seismol. Res. Lett.* 88, 392–409. <https://doi.org/10.1785/0220160191>.
- Reiss, M.C., Long, M.D., Creasy, N., 2019. Lowermost mantle anisotropy beneath Africa from differential SKS-SKKS shear-wave splitting. *J. Geophys. Res., Solid Earth* 124, 8540–8564. <https://doi.org/10.1029/2018JB017160>.
- Ritsema, J., Deuss, A., van Heijst, H.J., Woodhouse, J.H., 2011. S40RTS: a degree-40 shear-velocity model for the mantle from new Rayleigh wave dispersion, teleseismic traveltimes and normal-mode splitting function measurements. *Geophys. J. Int.* 184, 1223–1236. <https://doi.org/10.1111/j.1365-246X.2010.04884.x>.
- Sigloch, K., McQuarrie, N., Nolet, G., 2008. Two-stage subduction history under North America inferred from finite-frequency tomography. *Nat. Geosci.* 1, 458–462. <https://doi.org/10.1038/ngeo231>.
- Silver, P.G., Chan, W.W., 1991. Shear wave splitting and subcontinental mantle deformation. *J. Geophys. Res., Solid Earth* 96, 16429–16454. <https://doi.org/10.1029/91JB00899>.
- Stackhouse, S., Brodholt, J.P., Wookey, J., Kendall, J.M., Price, G.D., 2005. He effect of temperature on the seismic anisotropy of the perovskite and post-perovskite polymorphs of MgSiO₃. *Earth Planet. Sci. Lett.* 230, 1–10. <https://doi.org/10.1016/j.epsl.2004.11.021>.
- Suzuki, Y., Kawai, K., Geller, R.J., 2021. Imaging paleoslabs and inferring the Clapeyron slope in D'' beneath the northern Pacific based on high-resolution inversion of seismic waveforms for 3-D transversely isotropic structure. *Phys. Earth Planet. Inter.*, 106751. <https://doi.org/10.1016/j.pepi.2021.106751>.
- Tesoniero, A., Leng, K., Long, M.D., Nissen-Meyer, T., 2020. Full wave sensitivity of SK(K)S phases to arbitrary anisotropy in the upper and lower mantle. *Geophys. J. Int.* 222, 412–435. <https://doi.org/10.1093/gji/ggaa171>.
- Trabant, C., Hutko, A.R., Bahavar, M., Karstens, R., Ahern, T., Aster, R., 2012. Data products at the IRIS DMC: stepping stones for research and other applications. *Seismol. Res. Lett.* 83, 846–854. <https://doi.org/10.1785/0220120032>.
- Vinnik, L., Farra, V., Romanowicz, B., 1989. Observational evidence for diffracted SV in the shadow of the Earth's core. *Geophys. Res. Lett.* 16, 519–522. <https://doi.org/10.1029/GL016i006p00519>.
- Walker, A., Wookey, J., 2012. MSAT - a new toolkit for the analysis of elastic and seismic anisotropy. *Comput. Geosci.* 49, 81–90. <https://doi.org/10.1016/j.cageo.2012.05.031>.
- Walker, A.M., Forte, A.M., Wookey, J., Nowacki, A., Kendall, J.M., 2011. Elastic anisotropy of D'' predicted from global models of mantle flow. *Geochem. Geophys. Geosyst.* 12. <https://doi.org/10.1029/2011GC003732>.
- Walsh, E., Arnold, R., Savage, M.K., 2013. Silver and Chan revisited. *J. Geophys. Res., Solid Earth* 118, 5500–5515. <https://doi.org/10.1002/jgrb.50386>.
- Wentzcovitch, R.M., Tsuchiya, T., Tsuchiya, J., 2006. MgSiO₃ postperovskite at D'' conditions. *Proc. Natl. Acad. Sci. USA* 103, 543–546. <https://doi.org/10.1073/pnas.0506879103>.
- Wessel, P., Smith, W.H.F., 1998. New, improved version of generic mapping tools released. *Eos* 79, 579. <https://doi.org/10.1029/98EO00426>.
- Wolf, J., Creasy, N., Pisconti, A., Long, M.D., Thomas, C., 2019. An investigation of seismic anisotropy in the lowermost mantle beneath Iceland. *Geophys. J. Int.* 219, S152–S166. <https://doi.org/10.1093/gji/ggz312>.
- Wolf, J., Evans, D.A.D., 2022. Reconciling supercontinent cycle models with ancient subduction zones. *Earth Planet. Sci. Lett.*, 117293. <https://doi.org/10.1016/j.epsl.2021.117293>.
- Wolf, J., Long, M.D., Leng, K., Nissen-Meyer, T., 2022a. Constraining deep mantle anisotropy with shear wave splitting measurements: challenges and new measurement strategies. *Geophys. J. Int.* 230 (1), 507–527. <https://doi.org/10.1093/gji/ggac055>.

- Wolf, J., Long, M.D., Leng, K., Nissen-Meyer, T., 2022b. Sensitivity of SK(K)S and ScS phases to heterogeneous anisotropy in the lowermost mantle from global wavefield simulations. *Geophys. J. Int.* 228, 366–386. <https://doi.org/10.1093/gji/ggab347>.
- Wookey, J., Kendall, J.M., Rumpker, G., 2005a. Lowermost mantle anisotropy beneath the North Pacific from differential S-ScS splitting. *Geophys. J. Int.* 161, 829–838. <https://doi.org/10.1111/j.1365-246X.2005.02623.x>.
- Wookey, J., Stackhouse, S., Kendall, J.M., Brodholt, J., Price, G., 2005b. Efficacy of the post-perovskite phase as an explanation for lowermost-mantle seismic properties. *Nature* 438, 1004–1007. <https://doi.org/10.1038/nature04345>.
- Yu, S., Garnero, E.J., 2018. Ultralow velocity zone locations: a global assessment. *Geochem. Geophys. Geosyst.* 19 (2), 396–414. <https://doi.org/10.1002/2017GC007281>.
- Zhu, H., Komatitsch, D., Tromp, J., 2017. Radial anisotropy of the North American upper mantle based on adjoint tomography with USArray. *Geophys. J. Int.* 211, 349–377. <https://doi.org/10.1093/gji/ggx305>.
- Zhu, H., Yang, J., Li, X., 2020. Azimuthal anisotropy of the North American upper mantle based on full waveform inversion. *J. Geophys. Res., Solid Earth* 125, e2019JB018432. <https://doi.org/10.1029/2019JB018432>.